Fast Globally Optimal Segmentation of 3D Prostate MRI with Axial Symmetry Prior

Wu Qiu, Jing Yuan, Eranga Ukwatta, Yue Sun,
Martin Rajchl, and Aaron Fenster

Robarts Research Institute, University of Western Ontario, Canada

Abstract. We propose a novel global optimization approach to segmenting a given 3D prostate T2w magnetic resonance (MR) image, which enforces the inherent axial symmetry of the prostate shape and simultaneously performs a sequence of 2D axial slice-wise segmentations with a global 3D coherence prior. We show that the proposed challenging combinatorial optimization problem can be solved globally and exactly by means of convex relaxation. With this regard, we introduce a novel coupled continuous max-flow model, which is dual to the studied convex relaxed optimization formulation and leads to an efficient multiplier augmented algorithm based on the modern convex optimization theory. Moreover, the new continuous max-flow based algorithm was implemented on GPUs to achieve a substantial improvement in computation. Experimental results using public and in-house datasets demonstrate great advantages of the proposed method in terms of both accuracy and efficiency.

Keywords: Prostate MRI segmentation, axial symmetry, convex optimization.

1 Introduction

Prostate cancer is the most common non-skin cancer in men of developed countries [1]. Recent developments of prostate biopsy systems by fusing 3D TRUS images with MR images demonstrated increased positive yields and greater number of cores with higher Gleason grade[2]. Based on 3D TRUS-MRI registration, these techniques provide an alternative to the expansive MRI-based prostate biopsy by indirectly targeting biopsy needles toward prostate regions containing suspicious lesions identified with MR imaging. With this respect, an efficient and accurate prostate segmentation of the 3D prostate MR image is highly desired for such a 3D MRI to TRUS registration procedure. In addition, MR guided focal therapies can also benefit from this technique since an accurate prostate identification in 3D MR image is the crucial step of therapy planning [3].

Even though there existed extensive studies of delineating the prostate boundaries from 3D MR images, the segmentation of *in vivo* 3D T2w prostate MR images is still challenging due to the widely distributed high-contrast image edges and intensity inhomogeneities. Most studies of the automated or semi-automated

segmentation of 3D prostate MRIs rely on classifiers, atlas or deformable models (see [4,5]), which usually cannot meet the requirements on both efficiency and accuracy for the clinical routine. To this end, additional information about prostate shapes can greatly help locating the right prostate surfaces in practice. Such shape priors can be often learned through a specific training data-set [6]. However, the wide variety of prostate shape appearances often makes the learning step a computationally intensive task, especially for the 3D prostate shape representations. The axial symmetry of prostate has been applied to the segmentation of 3D prostate TRUS images [7], for which the segmentation of one 2D slice was propagated to assist segmenting its succeeding slice. Such propagation procedures often carry the segmentation errors in one slice to the segmentation of the following slices, thus causing an accumulated bias in all followed segmentations. On the other hand, the segmentation result of any slice has no contribution on refining the segmentation of its preceding slices.

Contributions. In this study, we introduce a rotational-resliced based approach to segmenting 3D prostate MRIs, which explores the inherent *axial symmetry* of the prostate shape. We propose a novel global optimization method to jointly segment all the generated 2D MRI slices while enforcing the introduced axial symmetry or rotational coherence along the specified axis. We show that the resulted combinatorial optimization problem can be optimized globally and exactly by means of convex relaxation.

2 Methodology

Initialization: The given 3D prostate MR image is first resliced rotationally around a specified axis in a transverse view (see the red dashed line in Fig. 1(b) for illustration) to 30 2D slices with the reslicing step angle of 6°. The rotational axis needs to be selected manually if the prostate is not in the middle of the image, making that all resliced 2D prostate contours intersect approximately along the rotational axis and have an equal angular spacing. Then, the user visually identifies the approximate prostate centroid on the first resliced transverse view; and a 2D mean shape, learned from 20 manually segmented 2D prostate transverse MR images, is aligned by the specified centroid, where the intensity appearance models, e.g. the probability density functions (PDF), of the prostate region and the background region are approximated by the voxels inside and outside the mean shape respectively.

Optimization Formulation with Axial Symmetry Prior: Let $\mathcal{V}$ be the input 3D prostate MR image, which is resliced rotationally along a given axis (red star in Fig. 1(a) and the red dashed line in Fig. 1(b)) to n 2D images $\mathcal{S}_1$ $\ldots \mathcal{S}_n$ (white lines in Fig. 1(a)). The 3D prostate surface can be reconstructed once the n 2D contours are correctly extracted. The shape of prostate allows the specification of the rotation axis, such that the prostate regions in every two adjacent slices are spatially consistent, i.e. the *axial symmetry prior*. In this section, we propose a novel and efficient global optimization approach to
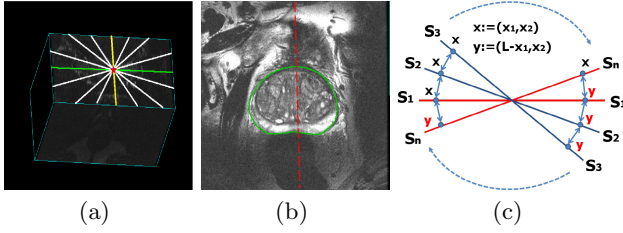
Fig. 1. Initialization scheme: (a) n resliced slices from the coronal view: rotation axis (red star), transverse view (green line), saggital view (yellow line) other resliced slices (white lines); (b) the rotational axis (red dash-line) is specified to reslice the input volume on a prostate transverse view (prostate boundary in green); (c) the initial and the last slices are colored in red and spatially correlated by left-right flipping.

simultaneously extract the n prostate contours from the 2D slices $\mathcal{S}_1 \ldots \mathcal{S}_n$ by jointly enforcing their *axial symmetry prior*.

Let $\mathcal{R}_i$, $i = 1 \ldots n$, denote the prostate region of the 2D slice $\mathcal{S}_i$, and $u_i(x) \in \{0, 1\}$, $i = 1 \ldots n$, be the indicator or labeling function of the region $\mathcal{R}_i$. The segmentation of each slice $\mathcal{S}_i$, $i = 1 \ldots n$, can be formulated as a spatially continuous min-cut problem [8] such that

$$\min_{u_i(x) \in \{0,1\}} E_i(u_i) := \langle 1 - u_i, C_i^s \rangle + \langle u_i, C_i^t \rangle + \int_\Omega g_i(x) \, |\nabla u_i| \; dx \qquad (1)$$

where the two cost functions $C_i^s(x)$ and $C_i^t(x)$ define the costs to label each pixel $x \in \mathcal{S}_i$ as the prostate region and background respectively. Moreover, the weighted total-variation function of (1) measures the smoothness of the region indicated by the labeling function $u_i(x) \in \{0, 1\}$, $i = 1 \ldots n$.

In this work, the n slices $\mathcal{S}_1 \ldots \mathcal{S}_n$ are simply aligned along the specified rotation axis, such that the rotational axis (see the red dotted line in Fig.1(b)). We propose to enforce the *axial symmetry prior* of prostate by penalizing the spatial inconsistency of the extracted prostate regions within two adjacent slices:

$$\pi_i(u) := \int_\Omega |u_{i+1} - u_i| \; dx, \quad i = 1 \ldots n - 1, \qquad (2)$$

and the spatial differences of $\mathcal{R}_n$ and $\mathcal{R}_1$ within the last and first slices:

$$\pi_n(u) := \int_\Omega |u_n(L - x_1, x_2) - u_1(x_1, x_2)| \; dx \qquad (3)$$

where $x := (x_1, x_2)$ and the spatial comparison is performed by left-right flipping the horizontal coordinates of the last slice, as shown in Fig.1(c).

In view of (1), (2) and (3), we propose to segment the n 2D image slices while incorporating their *axial symmetry prior*, such that

$$\min_{u_{1 \ldots n}(x) \in \{0,1\}} \sum_{i=1}^{n} E_i(u_i) + \alpha \sum_{i=1}^{n} \pi_i(u), \qquad (4)$$
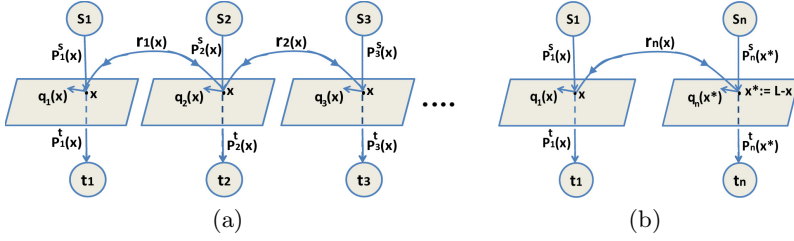
Fig. 2. (a) shows the flow-maximization configuration between two adjacent slices; (b) shows the flow-maximization configuration between the last and first slices.

where α is a parameter weighting the symmetry prior ($\alpha = 0.05$ in our experiments).

Convex Relaxation and Continuous Max-Flow Approach: We demonstrate that the proposed optimization problem (4) can be globally and exactly solved by its convex relaxation

$$\min_{u_{1\ldots n}(x)\in[0,1]} \sum_{i=1}^{n} E_i(u_i) + \alpha \sum_{i=1}^{n} \pi_i(u) \tag{5}$$

where the binary-valued constraints $u_{1\ldots n}(x) \in \{0,1\}$ in (4) is replaced by its convex relaxation $u_{1\ldots n}(x) \in [0,1]$. We study the convex optimization problem (5) under the primal and dual perspective, for which we introduce a new *coupled continuous max-flow model* and demonstrate that it is dual or equivalent to (5). With help of the proposed *coupled continuous max-flow model*, we prove that the computed global optimum of the convex relaxation problem (5) can also be used to solve its original combinatorial optimization problem (4) globally and exactly. In addition, a new *coupled continuous max-flow* algorithm can be derived.

We first introduce the new spatially continuous flow configuration (as illustrated in Fig. 2 (a) and (b)): For each image slice $\mathcal{S}_i$, $i = 1\ldots n$, two additional flow terminals: the source s_i and the sink t_i, are added. We link the source s_i to each pixel x in $\mathcal{S}_i$ and there is a flow $p_i^s(x)$ streaming from s_i to x. We also link each pixel $x \in \mathcal{S}_k$ to the sink t_i and there is a flow $p_k^t(x)$ streaming from x to t_i; within $\mathcal{S}_i$, there is a local vector flow field $q_i(x) \in \mathbb{R}^2$ around x. Between two adjacent slices $\mathcal{S}_i$ and $\mathcal{S}_{i+1}$, $i = 1\ldots n-1$, we link $x \in \mathcal{S}_i$ to the same pixel $x \in \mathcal{S}_{i+1}$ and there is a flow $r_i(x)$ streaming in both directions. Between the last slice $\mathcal{S}_n$ and the first slice $\mathcal{S}_1$, we link the pixel $x := (x_1, x_2) \in \mathcal{S}_1$ to the pixel $(L - x_1, x_2) \in \mathcal{S}_n$ and there is a flow $r_n(x)$ streaming in both directions.

With the above flow settings, we formulate the new coupled continuous max-flow model by maximizing the total amount of flows streaming from the n sources $s_1 \ldots s_n$, such that

$$\max_{p^s, p^t, q, r} \sum_{i=1}^{n} \int_{\Omega} p_i^s(x)\, dx \tag{6}$$

subject to the following flow-capacity constraints

$$p_i^s(x) \leq C_i^s(x) \,, \; p_i^t(x) \leq C_i^t(x) \,, \; |q_i(x)| \leq g_i(x) \,; \; i = 1 \ldots n \,; \tag{7}$$

$$|r_i(x)| \leq \alpha \,, \; i = 1 \ldots n \,; \tag{8}$$

the flow conservation constraints on the slices $\mathcal{S}_i$, $i = 2 \ldots n$:

$$\rho_i(x) := \big(\operatorname{div} q_i - p_i^s + p_i^t + r_i - r_{i-1} \big)(x) = 0 \,; \tag{9}$$

and flow conservation constraints on the first slice $\mathcal{S}_1$:

$$\rho_1(x) := \big(\operatorname{div} q_1 - p_1^s + p_1^t + r_1 \big)(x) - r_n(L - x_1, x_2) = 0 \,. \tag{10}$$

By introducing the multiplier functions $u_i(x)$, $i = 1 \ldots n$, to the linear equalities (10) and (9), we obtain the equivalent primal-dual model of (6):

$$\min_{u_1 \ldots u_n} \max_{p^s, p^t, q, r} \sum_{i=1}^{n} \int_{\Omega} p_i^s(x) \, dx + \sum_{i=1}^{n} \langle u_i, \rho_i \rangle \tag{11}$$

subject to the flow capacity constraints (7) - (8).

Through variational analysis (as in [8]), we can prove: I) the coupled continuous max-flow model (6), the convex relaxation problem (5) and the primal-dual model (11) are equivalent to each other; II) the optimum of the convex relaxation problem (5) is just given by the optimal multipliers to the corresponding flow conservation conditions (9)-(10), which directly derives an efficient *coupled continuous max-flow algorithm* by augmented Lagrangian algorithms. The proofs for these two proposition are omitted due to the limited space.

3   Implementation and Experiments

Image Acquisitions: We validated our algorithm using the publicly available dataset from 2012 MICCAI challenge [9], which comprises of 26 MR images acquired in a clinical setting. The data is multi-center and multi-vendor and has different acquisition protocols (*e.g.* differences in slice thickness, with/without endorectal coil). The proposed algorithm was also evaluated on 20 T2w images acquired in our institution. All subjects were scanned at 3.0T by a GE Excite HD MRI system (Milwaukee, WI, USA). 10 images were acquired with a body coil at a size of $512 \times 512 \times 36$ voxels (voxel size: $0.27 \times 0.27 \times 2.2$ mm^3), and 10 more were acquired with an endo-rectal coil using the same voxel size.

Evaluation Metrics: The experiment results were evaluated by the Dice similarity coefficient (DSC), the mean absolute surface distance (MAD) and maximum absolute surface distance (MAXD)[7]. In addition, 5 endocoil images and 5 bodycoil images from our dataset were randomly selected to evaluate the intra- and inter-observer variability of the proposed method caused by user initialization. Each image was segmented for 5 times by the first observer for assessing
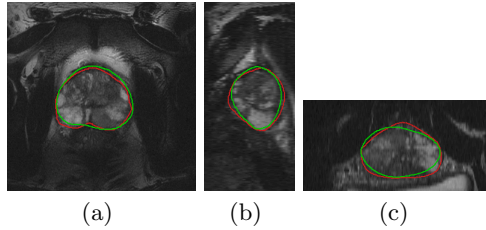
Fig. 3. Segmentation of one 3D MR image, *green*: the computed segmentation result, *red*: manual segmentation; (a) transverse view; (b) sagittal view; (c) coronal view.

the intra-operator variability. The mean run time of 5 repeated segmentations for each image was considered as the segmentation time used to evaluate the algorithmic efficiency. These 10 images were also segmented by three observers for evaluating the inter-observer variability. The coefficient of variation (CV) of DSC was used as the metric for assessing the intra-observer and inter-observer variability of the proposed method.

Accuracy and Reliability: Table 3 shows the segmentation results by the proposed method for three sets of 46 images: the proposed approach obtained a DSC of $85.2 \pm 4.5\%$ for the public dataset, $90.7 \pm 1.0\%$ for the bodycoil images, and $89.4 \pm 1.4\%$ for the endocoil images; the MAD and MAXD can also be found in the same Table. The intra-operator variability experiments yielded a DSC of $88.0 \pm 1.5\%$ and a CV of 1.7% for 5 segmentations from the same operator. ANOVA analysis with a single factor showed that there is no statistically significant difference between the three segmentations ($p = 0.61, F = 0.52$). In the intra-observer variability experiments, the proposed method yielded a DSC of $89.5 \pm 2.1\%$, $88.6 \pm 1.2\%$ and $90.3 \pm 2.2\%$, and a CV of 2.3%, 1.4% and 2.4% for the three observers respectively. ANOVA analysis with a single factor failed to demonstrate a statistically significant difference between these three segmentations ($p = 0.85, F = 0.90$).

Table 1. Overall performance results for public dataset and our datasets

	DSC (%)	MAD (voxel)	MAXD (voxel)
Public dataset (26 images)	85.2 ± 4.5	7.2 ± 2.3	16.7 ± 6.1
Body-coil images (10 images)	90.7 ± 1.0	6.3 ± 0.9	14.5 ± 2.6
Endo-coil images (10 images)	89.4 ± 1.4	6.4 ± 1.0	14.6 ± 3.0

Computational Time: The proposed *coupled max-flow algorithm* was implemented on GPU (CUDA, NVIDIA Corp., Santa Clara, CA) and the user interface was implemented in Matlab (Natick, MA). The experiments were performed on a Windows desktop with an Intel i7-2600 CPU (3.4 GHz) and a GPU of NVIDIA Geforce 5800X. The mean segmentation time of the proposed method

for all the images is 0.65 ± 0.15 sec, in addition to 4 ± 1 sec for initialization; so less than **5 sec** for segmenting a single 3D MR prostate image.

4   Discussion and Conclusions

We proposed a new global optimization algorithm to prostate segmentation from T2w MR images by enforcing the geometrically axial symmetry of prostate shapes, which jointly segments a series of 2D reslices under a global perspective. Experimental results with different datasets showed that the proposed method can segment the 3D prostate MR image within 5 seconds including 4 seconds for initialization, yielding a DSC of $90.7 \pm 1.0\%$. Another great advantage of our method is that it demonstrated robust against initialization. It should be noted that the proposed method is slightly sensitive to the parameter of the reslicing step, which is affected by image resolution: a small reslicing step results in a more accurate segmentation, while a large reslicing step leads to a less accurate segmentation. Therefore, the proposed method yielded a higher accuracy at our in-house dataset than the public dataset. In addition, the axial symmetry prior prevents the segmented 2D contours from leaking at locations of weak edges while keeping the spatial consistency between any adjacent 2D segmented contours. The soft constraint, i.e. the L1 penalty, of axial symmetry, in combination with the local image intensity and edge information, allows some asymmetric structure, such as tumors.

A direct quantitative comparison with the state-of-the-art methods in the literature is difficult due to the differences in used data and techniques. For example, the proposed method does not need training whereas some automatic methods [10] need a trained model to drive the segmentation. Thus, the experiments were performed in this paper to highlight the advantage of the proposed approach for prostate segmentation. For the public dataset, the highest mean DSC of $88.0 \pm 3.0\%$ for each image was reported in [11] using active appearance models, but the segmentation time was 8 minutes per image in addition 2 more hours for training. Compared to this method, the proposed approach performed with comparative accuracy, while demonstrating a great advantage in computational efficiency. Additionally, Yi *et al.*[12] reported a mean DSC of $84.0 \pm 3.0\%$ for their dataset, but did not report the segmentation time on their method of combined segmentation with registration. A mean DSC of 86.0% was reported for 36 cases in [10]. In this sense, $90.7 \pm 1.0\%$ for bodycoil images and $89.4 \pm 1.4\%$ for endocoil images obtained by the proposed approach is favourable in addition to its high computational efficiency compared to these methods[10,12]. Moreover, our experiment results also outperform the reported results by the 3D prostate segmentation method [13] with star-shape prior.

In conclusion, this paper provides an accurate and numerically efficient solution to a challenging 3D prostate MRI segmentation. The performance results of our algorithm demonstrate its promising application to 3D TRUS/MR image guided prostate interventions.

References

1. Jemal, A., Siegel, R., Xu, J., Ward, E.: Cancer statistics. CA Cancer J. Clin. 60(5), 277–300 (2010)
2. Leslie, S., Goh, A., Lewandowski, P.M., Huang, E.Y.H., de Castro Abreu, A.L., Berger, A.K., Ahmadi, H., Jayaratna, I., Shoji, S., Gill, I.S., Ukimura, O.: 2050 contemporary image-guided targeted prostate biopsy better characterizes cancer volume, gleason grade and its 3D location compared to systematic biopsy. The Journal of Urology 187(suppl. 3), e827 (2012)
3. Zini, C., Hipp, E., Thomas, S., Napoli, A., Catalano, C., Oto, A.: Ultrasound- and MR-guided focused ultrasound surgery for prostate cancer. World J. Radiol. 4(6), 247–252 (2012)
4. Ghose, S., Oliver, A., Martí, R., Lladó, X., Vilanova, J., Freixenet, J., Mitra, J., Sidibé, D., Meriaudeau, F.: A survey of prostate segmentation methodologies in ultrasound, magnetic resonance and computed tomography images. Computer Methods and Programs in Biomedicine (2012)
5. Toth, R., Madabhushi, A.: Multifeature landmark-free active appearance models: Application to prostate MRI segmentation. IEEE Transactions on Medical Imaging 31(8), 1638–1650 (2012)
6. Chandra, S., Dowling, J., Shen, K.K., Raniga, P., Pluim, J.P.W., Greer, P., Salvado, O., Fripp, J.: Patient specific prostate segmentation in 3-D magnetic resonance images. IEEE Transactions on Medical Imaging 31(10), 1955–1964 (2012)
7. Qiu, W., Yuan, J., Ukwatta, E., Tessier, D., Fenster, A.: Rotational-slice-based prostate segmentation using level set with shape constraint for 3D end-firing TRUS guided biopsy. In: Ayache, N., Delingette, H., Golland, P., Mori, K. (eds.) MICCAI 2012, Part I. LNCS, vol. 7510, pp. 537–544. Springer, Heidelberg (2012)
8. Yuan, J., Bae, E., Tai, X.: A study on continuous max-flow and min-cut approaches. In: CVPR 2010 (2010)
9. MICCAI: Grand challenge: Prostate MR image segmentation (October 2012)
10. Martin, S., Troccaz, J., Daanen, V.: Automated segmentation of the prostate in 3D MR images using a probabilistic atlas and a spatially constrained deformable model. Medical Physics 37, 1579 (2010)
11. Vincent, G., Guillard, G., Bowes, M.: Fully automatic segmentation of the prostate using active appearance models. In: MICCAI Challenge: Prostate MR Segmentation (2012)
12. Gao, Y., Sandhu, R., Fichtinger, G., Tannenbaum, A.: A coupled global registration and segmentation framework with application to magnetic resonance prostate imagery. IEEE Trans. Med. Imag. 29(10), 1781–1794 (2010)
13. Yuan, J., Qiu, W., Ukwatta, E., Rajchl, M., Sun, Y., Fenster, A.: An efficient convex optimization approach to 3D prostate mri segmentation with generic star shape prior. In: Prostate MR Image Segmentation Challenge, MICCAI 2012 (2012)